Preprints.org

Article

Not peer-reviewed version

Reactivity of Shale to Supercritical CO_2: Insights from SEM-EDS and Mineral Phase Evolution in Caney Shales for CCUS Applications

Loic Bethel Dje * and Mileva Radonjic *

Posted Date: 5 June 2025

doi: 10.20944/preprints202506.0412.v1

Keywords: geochemical CO2 sequestration; supercritical CO2; mineral trapping in shale

Preprints.org is a free multidisciplinary platform providing preprint service that is dedicated to making early versions of research outputs permanently available and citable. Preprints posted at Preprints.org appear in Web of Science, Crossref, Google Scholar, Scilit, Europe PMC.

Copyright: This open access article is published under a Creative Commons CC BY 4.0 license, which permit the free download, distribution, and reuse, provided that the author and preprint are cited in any reuse.

Preprints.org (www.preprints.org) | NOT PEER-REVIEWED | Posted: 5 June 2025 doi:10.20944/preprints202506.0412.v1

Disclaimer/Publisher's Note: The statements, opinions, and data contained in all publications are solely those of the individual author(s) and contributor(s) and not of MDPI and/or the editor(s). MDPI and/or the editor(s) disclaim responsibility for any injury to people or property resulting from any ideas, methods, instructions, or products referred to in the content.

Research Paper

Reactivity of Shale to Supercritical CO_2: Insights from SEM-EDS and Mineral Phase Evolution in Caney Shales for CCUS Applications

Loic Bethel Dje * and Mileva Radonjic *

Barrier Materials and Geomimicry Lab, School of Chemical Engineering, Oklahoma State University, Stillwater, OK 74078, USA

* Correspondence: lobethe@okstate.edu (L.B.D.); mileva.radonjic@okstate.edu (M.R.)

Abstract: Understanding mineral–fluid interactions in shale under supercritical CO_2 ($scCO_2$) conditions is relevant for assessing long-term geochemical containment. This study characterizes mineralogical transformations and elemental redistribution in five Caney Shale samples serving as proxies for reservoir (R1, R2, R3) and caprock (D1, D2) facies, subjected to 30-day static exposure to pure $scCO_2$ at 60 °C and 100 bars (2500 psi), with no brine or impurities introduced. SEM-EDS analyses were conducted before and after exposure, with mineral phases classified into silicates, carbonates, sulfides, and organic matter. Initial compositions were dominated by quartz (38–47 wt%), illite (16–23 wt%), carbonates (12–18 wt%), and organic matter (8–11 wt%). Post-exposure, carbonate loss ranged from 15–40% in reservoir samples and up to 20% in caprock samples. Illite and K-feldspar showed depletion of Fe^{2+}, Mg^{2+}, and K^{+} at grain edges and cleavages, while pyrite underwent oxidation with Fe redistribution. Organic matter exhibited $scCO_2$-induced surface alteration and apparent sorption effects, most pronounced in R2 and R3. Elemental mapping revealed Ca^{2+}, Mg^{2+}, Fe^{2+}, and Si^{4+} mobilization near reactive interfaces, though no secondary mineral precipitates formed. Reservoir samples developed localized porosity, whereas caprock samples retained more structural clay integrity. Results advance understanding of mineral reactivity and elemental fluxes in shale-based CO_2 sequestration.

Keywords: geochemical CO_2 sequestration; supercritical CO_2; mineral trapping in shale

1. Introduction

Geologic carbon sequestration (CCS) is a leading strategy for reducing atmospheric CO_2 levels through long-term storage in deep subsurface formations [1]. Shale formations, commonly utilized as caprocks, are now also being explored as storage media due to their fine-grained texture, high clay content, and nanoporous structure [2]. These characteristics enhance surface reactivity and support mechanisms such as sorptive trapping and geochemical immobilization.

Exposure of shale to supercritical CO_2 ($scCO_2$) can initiate a range of mineral-fluid interactions. Carbonate phases may undergo dissolution; phyllosilicates, particularly illite, can experience elemental leaching and structural disruption; and sulfides like pyrite may oxidize. These transformations can alter porosity, permeability, and long-term seal integrity [3,4]. Clay minerals are especially reactive due to their high surface area and exchangeable interlayer cations, which contribute to buffering and ion transport under $scCO_2$ conditions [5,6]. Additionally, $scCO_2$ has a higher diffusivity than water, allowing it to access internal shale surfaces more efficiently and drive reactions within nanopores and microfractures [7].

Previous studies have frequently incorporated brine or gas impurities, making it difficult to isolate the effects of CO_2 alone. Mineral transformations occur in shales under $scCO_2$–SO_2 conditions [8], but the independent behavior of shale minerals in the presence of pure CO_2 remains poorly

© 2025 by the author(s). Distributed under a Creative Commons CC BY license.

Preprints.org (www.preprints.org) | NOT PEER-REVIEWED | Posted: 5 June 2025 doi:10.20944/preprints202506.0412.v1

understood. Moreover, comparative data on reservoir and caprock lithofacies from the same shale formation under identical conditions are limited.

This study addresses that gap by examining mineralogical and geochemical changes in reservoir- and caprock-proxy samples from the Caney Shale after static exposure to pure $scCO_2$ at 60 °C and 2,000 psia for 30 days. Pre- and post-exposure characterization was performed using scanning electron microscopy with energy-dispersive X-ray spectroscopy (SEM-EDS), micro-computed tomography (microCT), and RAMAN spectroscopy to assess mineral phase changes, elemental redistribution, and structural modifications. The objective is to determine: (1) which mineral phases exhibit early-stage reactivity under pure $scCO_2$ conditions; (2) how reactivity differs between reservoir and caprock proxies; and (3) what microstructural features indicate the onset of mineral trapping or porosity evolution. By integrating SEM-EDS, microCT, and RAMAN spectroscopy with systematic phase classification across distinct lithofacies, this study establishes a baseline for understanding the intrinsic reactivity of shale formations under pure CO_2 conditions. The next section outlines the experimental setup, sample selection, and analytical procedures used to evaluate these transformations.

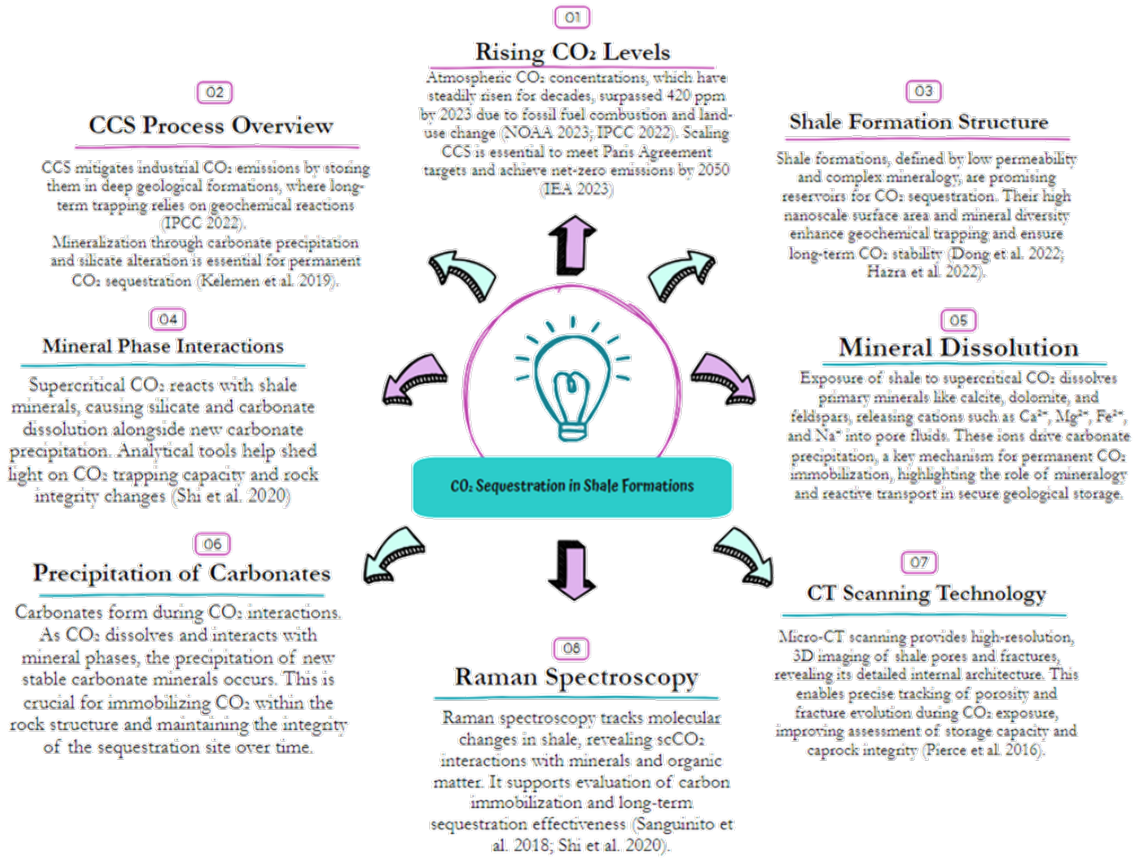

Figure 1. Summarized context of the research and the key questions our study answers.

Insights for literature review accounts for various research aspects, which our paper will seek to answer. Table 1. A summarized comprehensive literature.

Table 1. Literature review and gaps identified for a refined approach to our methodology.

Author(s)	Focus	Research Gaps
[9–11]	Numerical Simulations of CO_2 in Geological Settings	Limited empirical data on physicochemical interactions at the mineralogical level in shales. Need for experimental validation of simulated predictions and theoretical models.

© 2025 by the author(s). Distributed under a Creative Commons CC BY license.

Preprints.org (www.preprints.org) | NOT PEER-REVIEWED | Posted: 5 June 2025 doi:10.20944/preprints202506.0412.v1

[12,13]	Geologic Carbon Sequestration Review	High costs and energy requirements for CO_2 capture; need for cost reduction and efficiency enhancement.
[5,14,15]	Caprock Integrity and Fracture Dynamics	Need for long-term studies to understand the evolution of fissures under continuous CO_2 flow. Importance of considering hydrological factors in geological stability assessments.
[2,16–19]	Pore Structure Alterations	Microscale and nanoscale analysis, shale-specific studies, and controlled experiments are vital to assess structural changes and ensure long-term CO_2 storage integrity.
[5,7,20]	Subcritical and Supercritical CO_2 Effects on Shale	Robust simulations and further studies are essential to understand shale sensitivity to CO_2 under varying conditions and optimize EOR strategies.
[13,21–25]	CO2 Storage Capacity and Monitoring	Targeted modeling, localized studies, and field validation are essential to predict CO_2–shale interactions, refine capacity estimates, and assess long-term storage risks.
[5,9,19,26–34]	Impact of CO2 - Rock Interactions	Comprehensive experimental and modeling studies are needed to understand shale reactivity, nanoconfinement, water-chemistry interactions, and long-term CO_2 impacts across diverse geological settings.

2. Materials and Methods

Shale samples were sourced from the Caney Formation in Southern Oklahoma, representing fine-grained, organic-rich lithofacies. Two distinct zones were selected to represent reservoir and caprock analogs: Reservoir-proxy samples (R1, R2, R3) originated from the brittle zone and Caprock-proxy samples (D1, D2) came from the ductile zone.

Samples were cut and polished into 1 × 1 × 0.5 cm cubical for exposure to $scCO_2$. For each sample, two orientations were obtained: one parallel and one perpendicular to the bedding plane. This approach captured anisotropic responses to $scCO_2$ exposure. Each analyzed surface was further segmented into four quadrants and a central point (Point 5) to account for heterogeneity during post-exposure analysis.

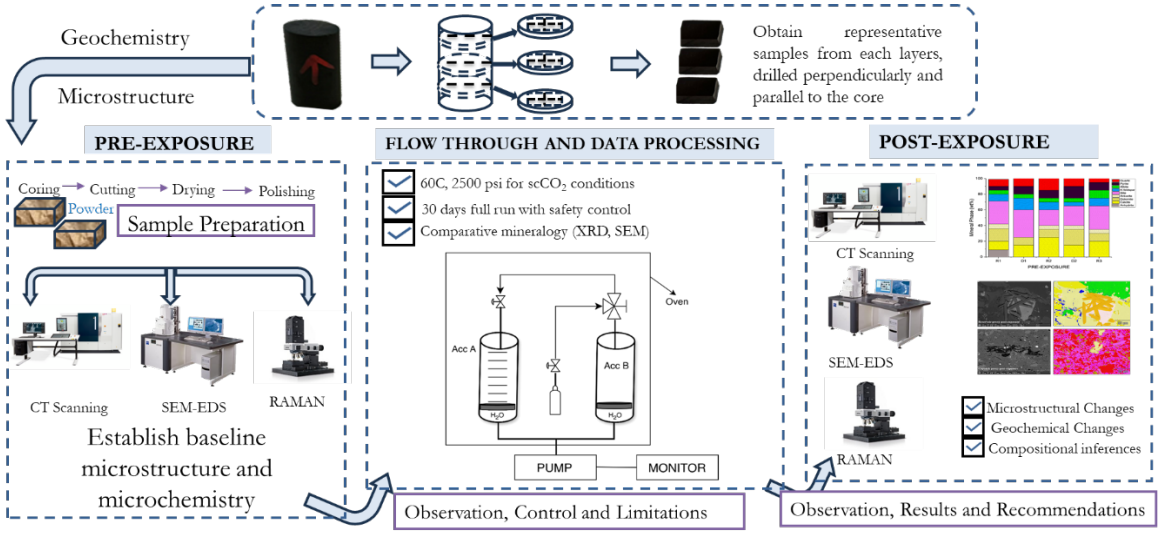

© 2025 by the author(s). Distributed under a Creative Commons CC BY license.

Preprints.org (www.preprints.org) | NOT PEER-REVIEWED | Posted: 5 June 2025 doi:10.20944/preprints202506.0412.v1

Figure 2. Comprehensive methodology. Accumulator B is filled with CO_2 and set to the supercritical conditions of 35°C and 1200 psi, and increased progressive in steps of 100psi and 5°C to reaction conditions (60 °C and 2500 psi). This is done with Acc A closed. Accumulator A contains the shelve on which the samples are stacked on trays, avoiding the any contaminations. Pressure is maintained using an Isco dual piston pump.

Pre and Post-exposure characterization involved a combination of imaging and spectroscopic methods to evaluate structural and chemical alterations (Figure 3). Due to the scale of interpretation, the CT scan wasn't adequate for this experiment and next experiments we plan to employ nano-CT. Samples were analyzed using scanning electron microscopy with energy-dispersive X-ray spectroscopy (SEM-EDS). Quadrant-based mapping and a central point (Point 5) were examined at magnifications ranging from 500× to 5,000×. Phases were classified as silicates (quartz, illite, feldspar), carbonates (calcite, dolomite), sulfides (pyrite), and organic matter. Elemental maps were used to track Fe, Mg, Ca, Si, K, and Al redistribution. Micro-computed tomography was used to evaluate internal porosity and structural evolution at high resolution. Pre- and post-exposure scans were performed to compare structural changes. RAMAN analysis was conducted using 532 nm and 785 nm lasers at ~1 µm resolution over a 1x1 cm area. This method identified shifts in carbonate peak positions, disordering in clay mineral structures, and potential alterations in organic matter. Spectra were collected at 20x magnification to support correlation with SEM-EDS data.

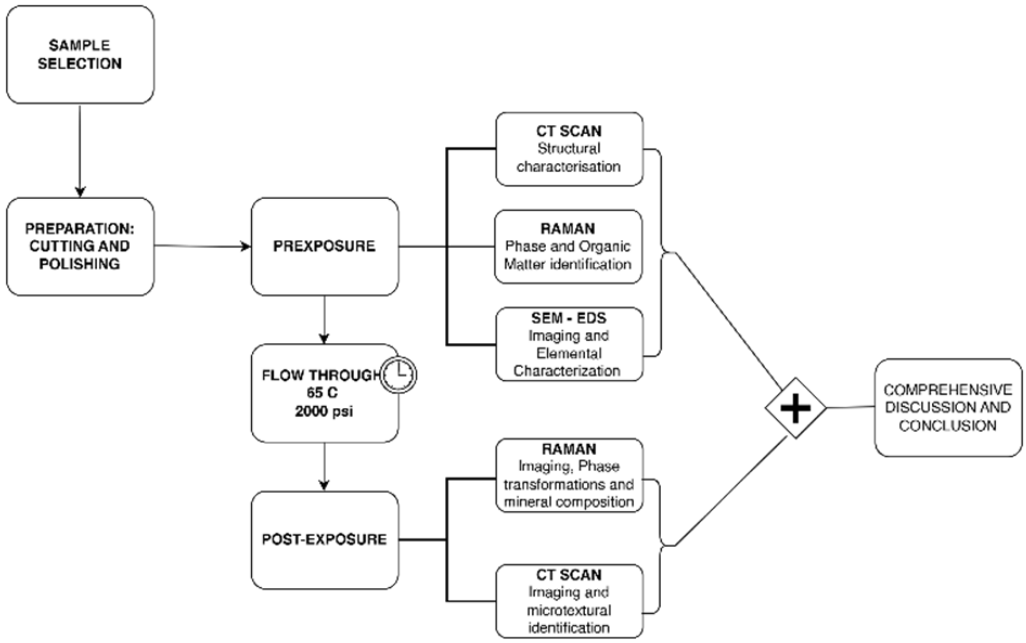

Figure 3. Experimental flowchart, displaying the thought-process and symbiotic use of microscopy and spectroscopy for phase identification and experimental validity.

3. Results

Post-exposure SEM-EDS analyses revealed distinct mineralogical changes across reservoir and caprock facies, driven by phase-specific reactivity to $scCO_2$. This section details the identified mineral phases, their compositional shifts, and morphological alterations after 30-day exposure.

3.1. Mineral Phase Identification

Qualitative and morphological analyses from SEM-EDS revealed clear mineralogical heterogeneity across the Caney Shale facies. Samples were mapped at five locations per face four quadrants and a central point to ensure spatial representativity. SEM-backscattered imaging and EDS revealed distinct phase compositions and early-stage alterations across the Caney Shale samples after

© 2025 by the author(s). Distributed under a Creative Commons CC BY license.

Preprints.org (www.preprints.org) | NOT PEER-REVIEWED | Posted: 5 June 2025 doi:10.20944/preprints202506.0412.v1

30 days of pure $scCO_2$ exposure. Reservoir and caprock proxies showed both compositional heterogeneity and phase-specific responses following $scCO_2$ exposure. All five samples exhibited increases in organic matter visibility, while silicate and sulfate phases developed locally under reactive conditions. Primary mineral phases identified include quartz, illite, calcite, dolomite, K-feldspar, pyrite, and organic matter as shown in Figure 4, with a cross mineralogical comparison in Figure 5.

- Quartz remained the principal framework silicate across all facies. In reservoir proxies, pre-exposure abundances were 43.77% (R1), 42.23% (R2), and 45.96% (R3), with post-exposure values of 43.94%, 42.22%, and 45.68%, respectively. In caprock proxies, quartz accounted for 33.79% (D1) and 33.69% (D2) prior to exposure, increasing marginally to 34.13% and 32.75% post-exposure. Across all facies, quartz grains retained angular, sharp morphologies with no significantly observable structural or chemical alteration
- K-Feldspar ($KAlSi_3O_8$). K-feldspar was consistently present in all samples. In reservoirs, values ranged from 5.06% to 5.84% pre-exposure and from 5.89% to 5.99% post-exposure. In D1 and D2, K-feldspar was measured at 7.06% and 6.54% pre-exposure, increasing slightly to 7.13% and 6.36% post-exposure. No dissolution or surface roughening was evident under SEM imaging.
- Illite $[(K,H_3O)(Al,Mg,Fe)_2(Si,Al)_4O_{10}(OH)_2]$. Illite occurred in all facies and was typically distributed along grain boundaries or within clay-rich matrices. Pre-exposure content ranged from 17.61% (R3) to 18.40% (R2), and post-exposure values decreased slightly to 17.69%–18.67%. In ductile samples, illite was recorded at 17.26% (D1) and 16.68% (D2) before exposure, declining to 17.47% and 16.31%, respectively. Platy textures remained intact, although localized thinning and roughening of particle edges were noted in R2 and R3.
- Kaolinite ($Al_2Si_2O_5(OH)_4$). Kaolinite was identified in D1 and D2. Pre-exposure values were 10.03% (D1) and 9.89% (D2), increasing slightly to 10.13% and 9.76%, respectively, post-exposure. Kaolinite maintained blocky morphology with no signs of chemical erosion or micro-pitting.
- Paragonite ($NaAl_2(Si_3Al)O_{10}(OH)_2$). Paragonite was not detected in any sample prior to exposure. Post-exposure, it appeared in R2 (0.38%), R3 (0.88%), D1 (0.72%), and D2 (0.90%). It was typically observed near altered illite flakes and within fine-grained matrix zones, forming as secondary Na-bearing phyllosilicate lamella.
- Calcite ($CaCO_3$). Calcite was present in all samples, particularly in the reservoir facies. In R1–R3, calcite decreased slightly from 9.92%, 9.97%, and 8.80% pre-exposure to 9.01%, 8.76%, and 9.05%, respectively. In caprocks, it declined from 9.41% (D1) and 9.62% (D2) to 9.75% and 8.80%, respectively. SEM images revealed surface pitting and edge retreat, especially in R1 and R2.
- Ankerite $[Ca(Fe^{2+},Mg)(CO_3)_2]$. Ankerite occurred in both reservoir and caprock proxies. In R1–R3, pre-exposure values ranged from 4.40% to 5.49%, decreasing post-exposure to 4.08% – 4.33%. In D1, it was not detected pre-exposure and remained absent post-exposure. In D2, it decreased from 4.02% to 3.55%. Morphologies were retained but with localized surface dulling near grain boundaries.
- Wollastonite ($CaSiO_3$). Wollastonite was absent prior to exposure and formed in all samples post-exposure. In R1–R3, abundances were 0.67%, 1.08%, and 1.02%, respectively. In D1 and D2, wollastonite was recorded at 0.56% and 0.93%. It appeared as fibrous or acicular precipitates localized around sites of prior carbonate dissolution.
- Albite ($NaAlSi_3O_8$). Albite was present in every sample. Pre-exposure values in R1–R3 ranged from 4.88% to 5.96%, decreasing slightly to 5.75%–5.94% post-exposure. In D1 and D2, albite changed from 4.71% and 4.82% to 4.93% and 4.65%, respectively. Grains retained sharp outlines and showed no dissolution features.
- Pyrite (FeS_2). Pyrite was present across all facies. In reservoirs, pre-exposure values ranged from 4.88% (R1) to 5.87% (R2), declining to 4.67%–5.41% post-exposure. In D1 and D2, pyrite decreased from 6.28% and 6.26% to 5.56% and 4.84%, respectively. SEM showed edge diffusion and oxidation halos near OM and clay interfaces in caprock samples.

© 2025 by the author(s). Distributed under a Creative Commons CC BY license.

Preprints.org (www.preprints.org) | NOT PEER-REVIEWED | Posted: 5 June 2025 doi:10.20944/preprints202506.0412.v1

- Jarosite [$KFe_3(SO_4)_2(OH)_6$]. No jarosite was detected prior to exposure. It was identified post-exposure in R3 (0.58%), D1 (1.24%), and D2 (1.49%), with trace detection in R1. No formation was observed in R2. It formed as fine-grained aggregates, frequently bordering pyrite and organic-rich regions.
- Calcium Sulfate ($CaSO_4$). Calcium sulfate was not detected pre-exposure and was present only post-exposure in caprock samples: 0.80% in D1 and 1.07% in D2. It appeared as thin, patchy coatings at mineral boundaries.

Organic Matter (CxHyOz). Organic matter was found in all samples, increasing post-exposure in every case. In R1–R3, OM increased from 5.17%, 6.57%, and 5.99% pre-exposure to 10.79%, 12.77%, and 11.89%, respectively. In D1 and D2, OM rose from 6.66% and 6.99% to 12.15% and 14.19%, respectively. Post-exposure OM showed increased surface roughness, irregularity, and porosity development.

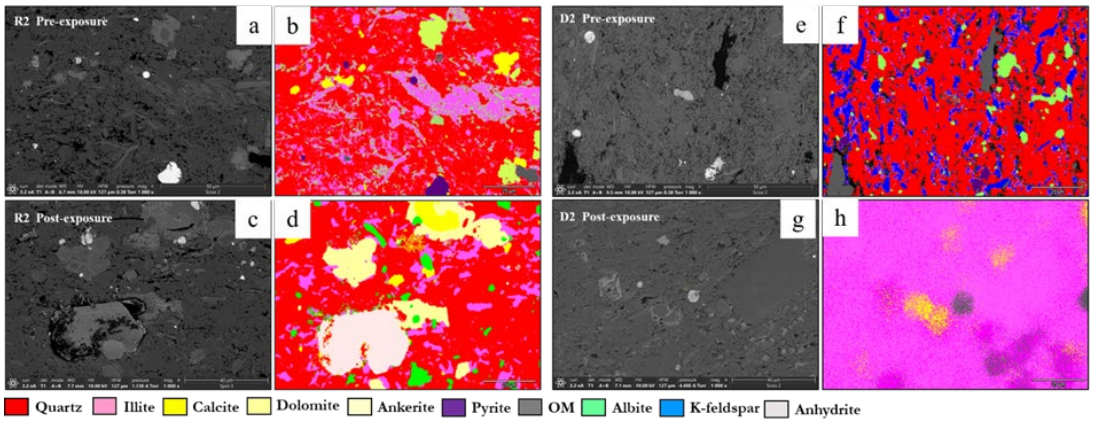

Figure 4. Mineral phase variability between reservoir and caprock proxies shown through SEM and mineral phase maps of R2 (a–d) and D2 (e–h) before and after $scCO_2$ exposure, illustrating facies-specific mineralogical transformations and implications for CO_2 sequestration. *R2 (a–d)* – The reservoir facies exhibit significant mineral reactivity, with pre-exposure assemblages of quartz, illite, anhydrite, albite, calcite, and ankerite transitioning to a more reactive post-exposure system marked by secondary dolomite, kaolinite, pyrite, and abundant organic matter. Widespread feldspar and carbonate dissolution, coupled with illite compositional changes, reflect active fluid–mineral interactions enhancing both porosity and mineral trapping potential. *D2A (e–h)* – In contrast, the caprock facies remains comparatively stable. While pre-exposure composition includes OM, illite (K and Na), and ankerite, post-exposure changes are more subdued, characterized by moderate growth in kaolinite and dolomite, persistence of illite, and limited carbonate transformation. This mineralogical resilience, dominated by low-permeability clays, supports long-term capillary sealing and geochemical buffering under dry $scCO_2$ conditions.

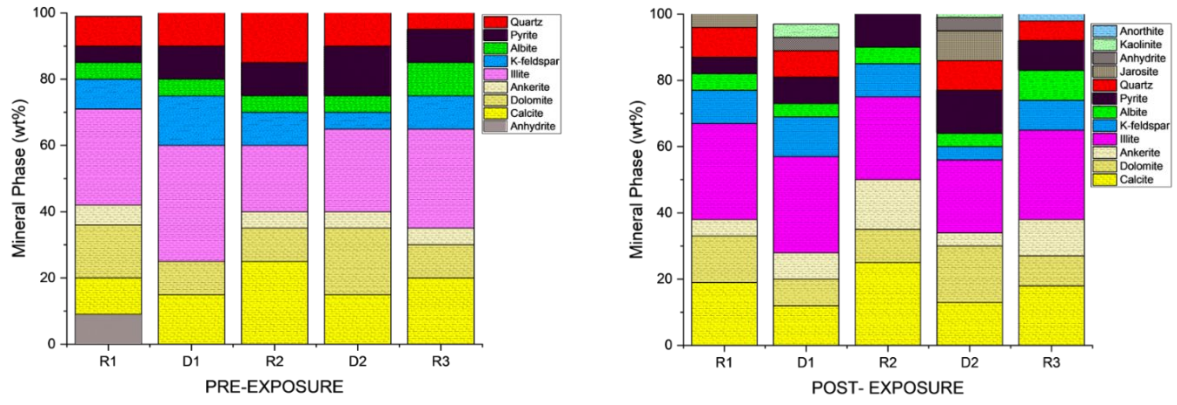

Figure 5. Mineral phase compositions pre and post CO_2 exposure for the reservoir and caprock proxies. In reservoirs, $scCO_2$ induced clear transformations: organic matter increased substantially (R2: 6.57% to 12.77%),

© 2025 by the author(s). Distributed under a Creative Commons CC BY license.

Preprints.org (www.preprints.org) | NOT PEER-REVIEWED | Posted: 5 June 2025 doi:10.20944/preprints202506.0412.v1

while calcite and ankerite declined (R2 calcite: −1.21%, ankerite: −1.16%). New phases such as dolomite, jarosite, and wollastonite emerged, indicating active carbonate alteration and secondary mineral formation. Quartz and illite remained relatively stable. In caprock proxies, changes were more restrained. Organic matter still rose sharply (D2: 6.99% to 14.19%), with minor reductions in calcite and pyrite, and the appearance of jarosite and calcium sulfate. Key clays (illite, kaolinite) and framework silicates showed minimal change, reflecting strong geochemical variations.

3.2. Elemental Mobilization

Variations in K^+, Ca^{2+}, Mg^{2+}, Na^+, SO_2^{4-}, and $Fe^{2+/3+}$ are recorded across R1. K^+ and Na^+ signals decrease alongside a reduction in K-feldspar abundance (13.6% to 10.2%) and Albite (5.0% to 3.4%). Ca^{2+} and Mg^{2+} shifts correspond to marked declines in Calcite (18.0% to 11.2%) and Ankerite (5.0% to 2.1%). SO_4^{2-} release is supported by the disappearance of Anhydrite (2.5% pre-exposure). A drop in Pyrite content (3.2% to 1.4%) aligns with trace-level Fe^{2+} observations. Illite (27%) and Quartz (24.7%) show no significant quantitative change. Minor components such as Kaolinite (<1.5%) remain within detection limits without notable shift.

Ionic reductions are inferred for K^+, Ca^{2+}, Mg^{2+}, SO_4^{2-}, and Fe^{2+} in D1. These align with the measured loss in K-feldspar (14.3% to 9.8%) and Illite (26.7% to 22.9%), as well as Calcite (15.4% to 9.3%) and Dolomite (12.2% to 8.0%). Sulfur-bearing phases show change, with Anhydrite declining from 3.0% to <1.0%. Pyrite decreases to 2.1%, and minor Fe signals are present in adjacent altered zones. Na^+ remains stable, with Albite retaining 3.2%. Quartz (24%) and minor phases such as Kaolinite and organic matter (1%) do not register significant variation.

In R2, changes in K^+, Ca^{2+}, Mg^{2+}, SO_4^{2-}, and Fe^{2+} are evident. K-feldspar content declines from 12.7% to 8.4%, and Illite from 21.9% to 19.2%. Calcite and Dolomite decrease to 10.1% and 6.3%, respectively, reflecting a reduction in Ca^{2+} and Mg^{2+} during carbonates reprecipitation. Anhydrite, originally present at 2.8%, is no longer detected post-exposure, consistent with increased SO_4^{2-} signal. Pyrite falls to 2.3%, with $Fe^{2+/3+}$ signal diffusion around previous grain boundaries. Albite (3%) and Na^+ levels remain stable. Quartz holds at 24.6%. Kaolinite (1.1%) and organic matter (0.9%) are preserved without apparent shifts.

The reduction of Ca^{2+}, Mg^{2+}, K^+, and SO_4^{2-} is confirmed across D2. This corresponds with decreased proportions of Calcite (17.5% to 11.6%), Dolomite (11.8% to 7.5%), and K-feldspar (13.2% to 8.9%). Illite shifts slightly (19.6% to 17.1%), while Anhydrite (2.6%) is fully absent post-exposure, with elevated sulfur signals noted in former anhydrite-bearing regions. Pyrite declines to 1.7%, with minor Fe presence. Albite ranges from 3.1% to 2.6%, with negligible Na^+ signal deviation. Quartz (~23.9%) and minor minerals such as Kaolinite, organic matter, and trace phosphates show no measurable alteration.

SEM-EDS elemental mapping indicates selective post-exposure mobilization of K^+, Ca^{2+}, Mg^{2+}, Fe^{2+}, and SO_4^{2-} across facies. Carbonate-bearing zones in R1, R2, and R3 show marked Ca^{2+} and Mg^{2+} depletion, consistent with mineral phase volume loss from Calcite, Dolomite, and Ankerite. Pyrite-associated $Fe^{2+/3+}$ and $S(SO_4^{2-})$ signals decrease, with partial redistribution observed in caprock proxies such as D2. Illite grains exhibit localized leaching of K^+, Mg^{2+}, and $Fe^{2+/3+}$, particularly in the reservoir proxies. In contrast, Si and Al remain stable, reflecting Quartz and K-feldspar persistence. Organic matter becomes more spatially distributed post-exposure, especially along former carbonate-clay boundaries. No secondary precipitates were detected within the 30-day interval, though surface alterations indicate potential reactivity under extended conditions. Figures 6 and 7 give a sample observation of a key feature observed post reaction for a caprock and reservoir proxy.

Table 2. From ionic mobilizations to sequestration, a summary of the potential ionic mobilizations.

Ionic Species	Primary Mineral Phase Sources	Facies Observed	Post-Exposure Observation	Possible Geochemical Path

© 2025 by the author(s). Distributed under a Creative Commons CC BY license.

Preprints.org (www.preprints.org) | NOT PEER-REVIEWED | Posted: 5 June 2025 doi:10.20944/preprints202506.0412.v1

K^+	K-feldspar, Illite	R1, R2, D1, D2, R3	K-feldspar reduction (13.6% to 7-10%); slight Illite shift	Leaching from feldspars and clay edges
Na^+	Albite	R1, R3, D2	Minor Albite decline (5.0% to 2.6-3.4%)	Limited Na^+ exchange
Ca^{2+}	Calcite, Dolomite, Ankerite	R1, R2, R3, D1, D2	Redistribution among carbonate phases; net Ca^{2+} preserved	Partial dissolution and re-precipitation
Mg^{2+}	Dolomite, Illite, Ankerite	R2, R3, D2, D1	Mg-bearing carbonates reduced; Dolomite often retained	Phase transition and reallocation
Fe^{2+} / Fe^{3+}	Pyrite, Illite, Ankerite	D1, D2, R2, R3	Pyrite decreased (up to 50%); Fe detected near former grains	Oxidation and surface destabilization
SO_4^{2-}	Anhydrite, Pyrite	R1, D1, D2, R2, R3	Anhydrite loss, S redistributed	Sulfate release from dissolution/oxidation
Al^{3+}	K-feldspar, Albite, Illite	All facies	No significant compositional change	Structurally retained in aluminosilicates
Si^{4+}	Quartz, K-feldspar, Illite, Albite	All facies	Quartz (~24–25%) stable throughout	Framework remains chemically inert
C (elemental) CO_3^{2-}	Calcite, Dolomite, Ankerite	All facies	Carbon and carbonates retained via phase shifts, not net loss	Re-precipitation or phase conversion
S (Elemental)	Pyrite, Anhydrite	D2, R2, R3	Sulfur detected post-Anhydrite; diffused spatially	Sulfate migration from sulfates/sulfides
P / PO_4^{3-}	Apatite, trace organics	D2, R3 (trace levels)	Stable in isolated inclusions	Largely inert under dry CO_2

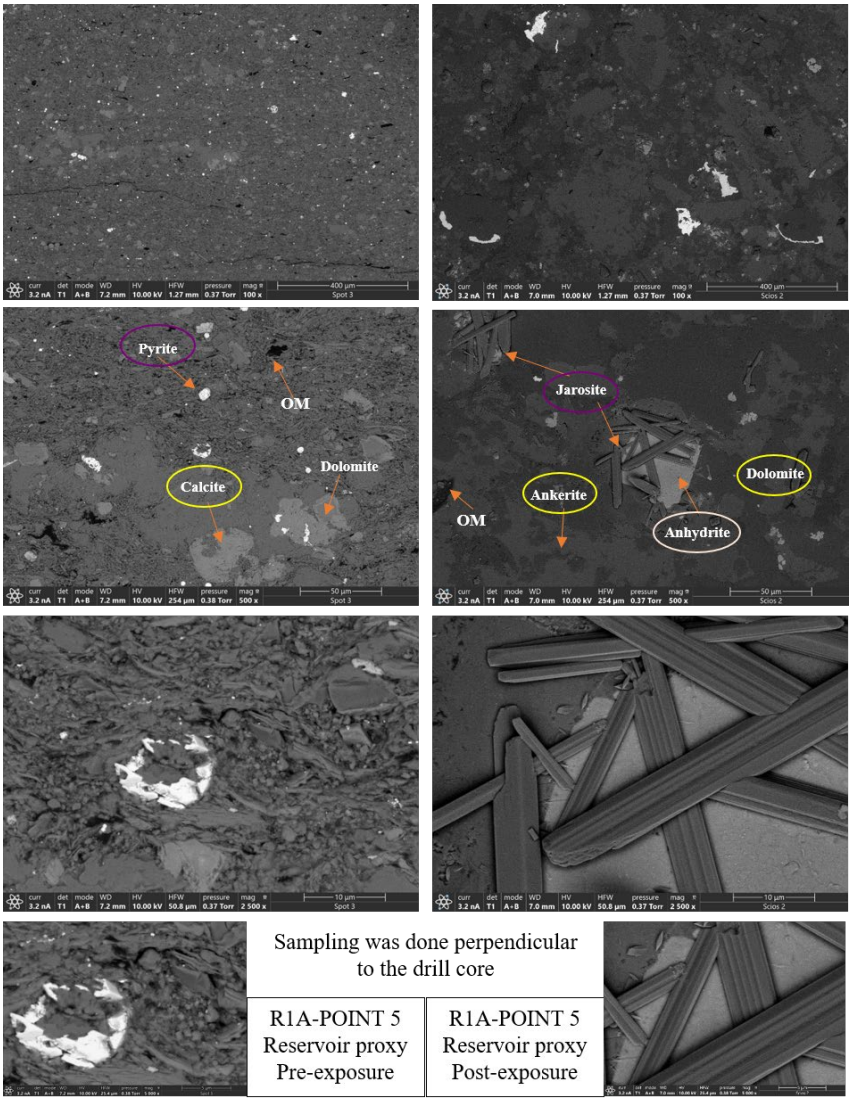

© 2025 by the author(s). Distributed under a Creative Commons CC BY license.

Preprints.org (www.preprints.org) | NOT PEER-REVIEWED | Posted: 5 June 2025 doi:10.20944/preprints202506.0412.v1

Figure 6. SEM of R1A–Point 5 (reservoir proxy) before (left) and after (right) scCO₂ exposure, showing mineralogical transformations. Pre-exposure images reveal calcite, dolomite, pyrite, and organic matter within a silicate framework. Post-exposure, new jarosite forms alongside dolomite, ankerite, and anhydrite near OM-rich zones. Jarosite, resulting from pyrite oxidation, enhances CO_2 trapping through sulfate crystallization, introduces micro-porosity, and contributes to grain-scale stability, highlighting its key role in long-term sequestration and reservoir reinforcement.

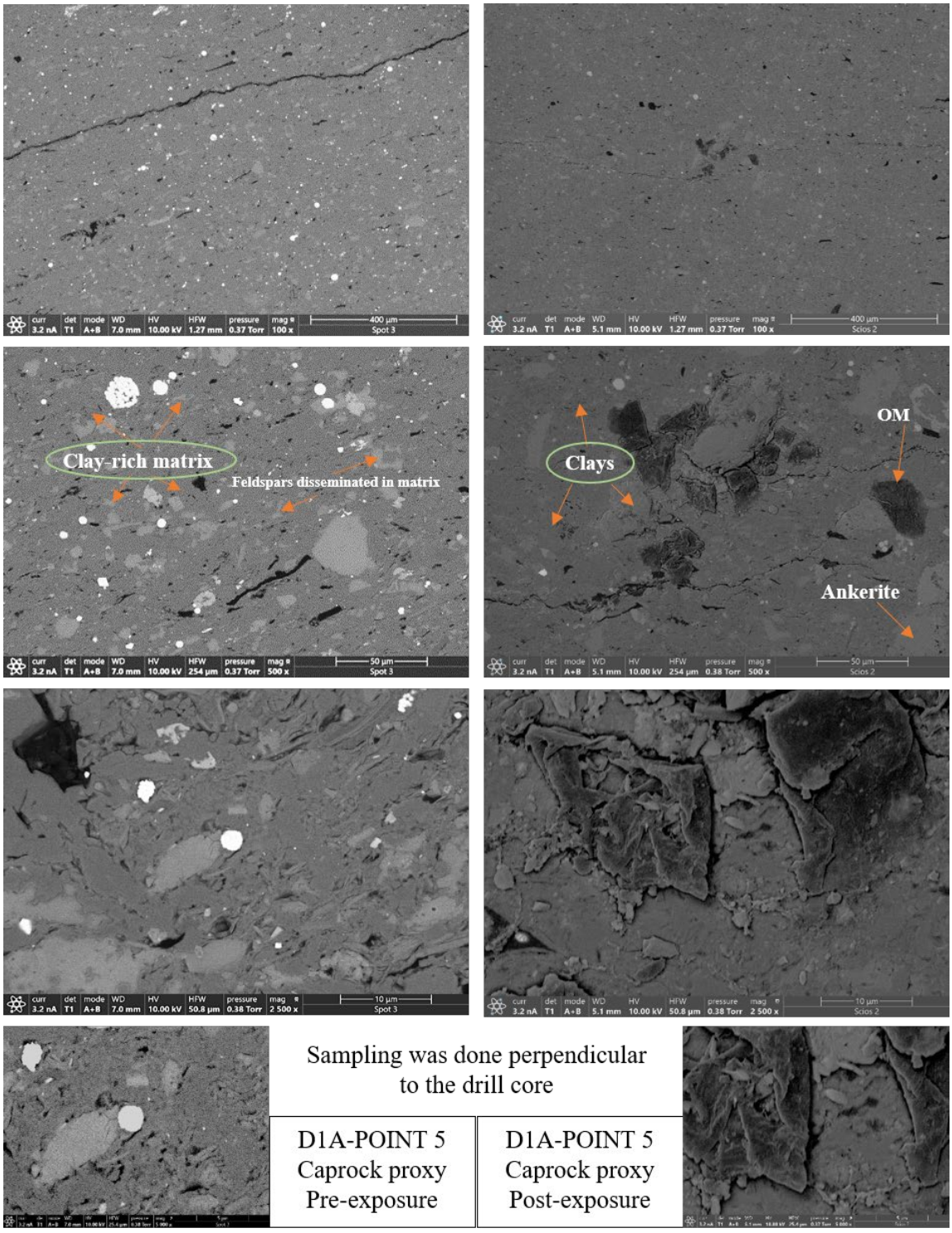

Figure 7. D1A Caprock proxy pre and post exposure. SEM images of D1A–Point 5 (caprock proxy) before (left) and after (right) scCO₂ exposure, showing textural and mineralogical changes. Pre-exposure images reveal a fine-grained, clay-rich matrix with disseminated feldspars. Post-exposure, the caprock surface shows enhanced expression of clays and feldspars, alongside preserved organic matter and ankerite. The increased concentration

© 2025 by the author(s). Distributed under a Creative Commons CC BY license.

Preprints.org (www.preprints.org) | NOT PEER-REVIEWED | Posted: 5 June 2025 doi:10.20944/preprints202506.0412.v1

of clays suggests mineral stabilization and enrichment, reinforcing the caprock's sealing capacity and long-term geochemical integrity following $scCO_2$ injection.

4. Discussion

4.1. Mineral Stability and Reactivity

The early-stage mineralogical and microstructural changes observed in the Caney Shale samples have important impact on the long-term safety and effectiveness of geologic carbon sequestration. The Caney Shale demonstrates that supercritical CO_2 ($scCO_2$) exposure initiates diverse mineralogical transformations, largely governed by facies-level differences in composition, porosity, and reactivity. While the broad categories of carbonate dissolution and clay interaction have been widely reported in other shales, this study reveals the importance of sulfate-related transformations and the catalytic role of organic matter. These findings support a nuanced understanding of geochemical reactivity across mechanically distinct lithologies [35] and provide some insights for carbon storage safety and long-term relevance.

4.1.1. Carbonate Phases

Reservoir facies such as R2A and R3A displayed extensive dissolution of calcite and ankerite. This pattern confirms earlier observations of carbonate reactivity under CO_2-rich conditions [36], where the release of Ca^{2+}, Mg^{2+}, and Fe^{2+} ions initiates buffering and supports the early stages of mineral trapping [37]. In contrast to previous findings where reprecipitation was considered minimal without brine [34], this study provides evidence of secondary precipitation even under nominally dry conditions. Carbonate reactivity is a major gateway to geochemical sequestration of CO_2. No discrete Ca-silicate phases such as wollastonite were identified. Ca–Si signals observed in Raman and EDS maps are likely attributable to mixed silicate-carbonate domains or poorly crystalline components associated with clay-carbonate interfaces [38]. Figure 8 is an illustration of these. The formation of calcium silicate (wollastonite) indicates that these carbonates did not simply dissolve but instead facilitated new stable mineral assemblages. Such transformations likely arise through coupled reactions involving silicate-structural and carbonate-derived cations [32]. Their spatial localization near feldspar-carbonate-OM boundaries suggests that geochemical trapping in Caney Shale is interface-driven rather than homogeneous. This behavior underscores the importance of interfacial mineralogy in shaping the spatial pattern of storage efficiency.

© 2025 by the author(s). Distributed under a Creative Commons CC BY license.

Preprints.org (www.preprints.org) | NOT PEER-REVIEWED | Posted: 5 June 2025 doi:10.20944/preprints202506.0412.v1

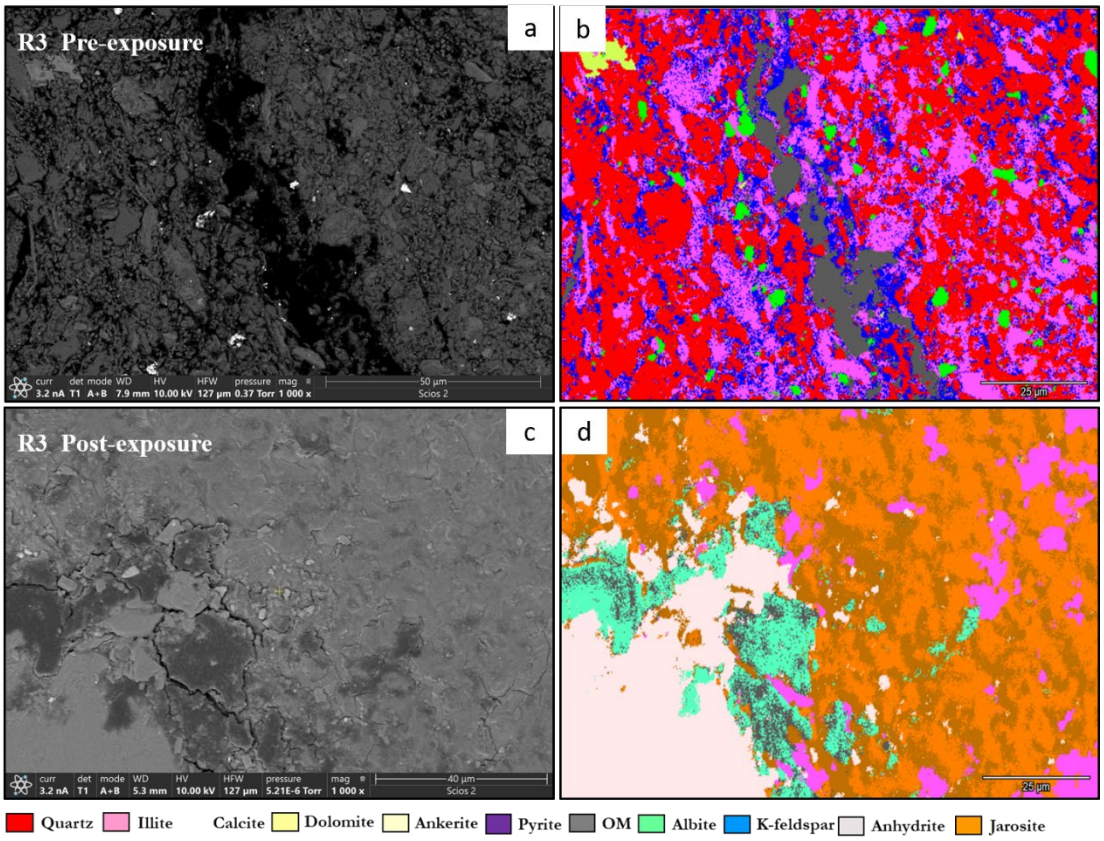

Figure 8. Mineral phase maps and backscattered images from R3A illustrating carbonate phase evolution. Post-exposure maps show partial replacement or reduction in ankerite and calcite at feldspar–carbonate interfaces, supporting evidence of localized carbonate.

4.1.2. Clays and Feldspars

Clay minerals exhibited distinct responses across facies. In the ductile caprock settings of D1 and D2, illite displayed edge thinning alongside localized transformation into paragonite, accompanied by an overall increase in illite presence. This trend is consistent with illitization, potentially driven by minor Na^+ availability from albite or residual interstitial fluids [30,39]. Alterations observed near clay boundaries under low-water conditions suggest that clay phases can undergo mineralogical adjustment, contrary to prior assumptions of their inert behavior in $scCO_2$ environments, particularly where thin water films persist [31,40]. The increased clay content, along with progressive illitization, is associated with enhanced ductility and greater sealing capacity in the caprock proxies [28,32]. Feldspars, while structurally preserved, show signs of active chemical exchange. Slight K^+ depletion and surface etching, particularly in R1A and R3A, point to early-stage hydrolysis [33]. These reactions may facilitate the formation of secondary clays or contribute mobile cations relevant to CO_2 trapping processes. The involvement of feldspars in such geochemical interactions reflects long-term alteration patterns observed in sedimentary basins [34], although their direct contribution to mineral trapping remains limited. Clays and feldspar serve as alteration controllers and ion exchange sites. Figure 9 illustrates the clay mobilization in the caprock proxy D1.

© 2025 by the author(s). Distributed under a Creative Commons CC BY license.

Preprints.org (www.preprints.org) | NOT PEER-REVIEWED | Posted: 5 June 2025 doi:10.20944/preprints202506.0412.v1

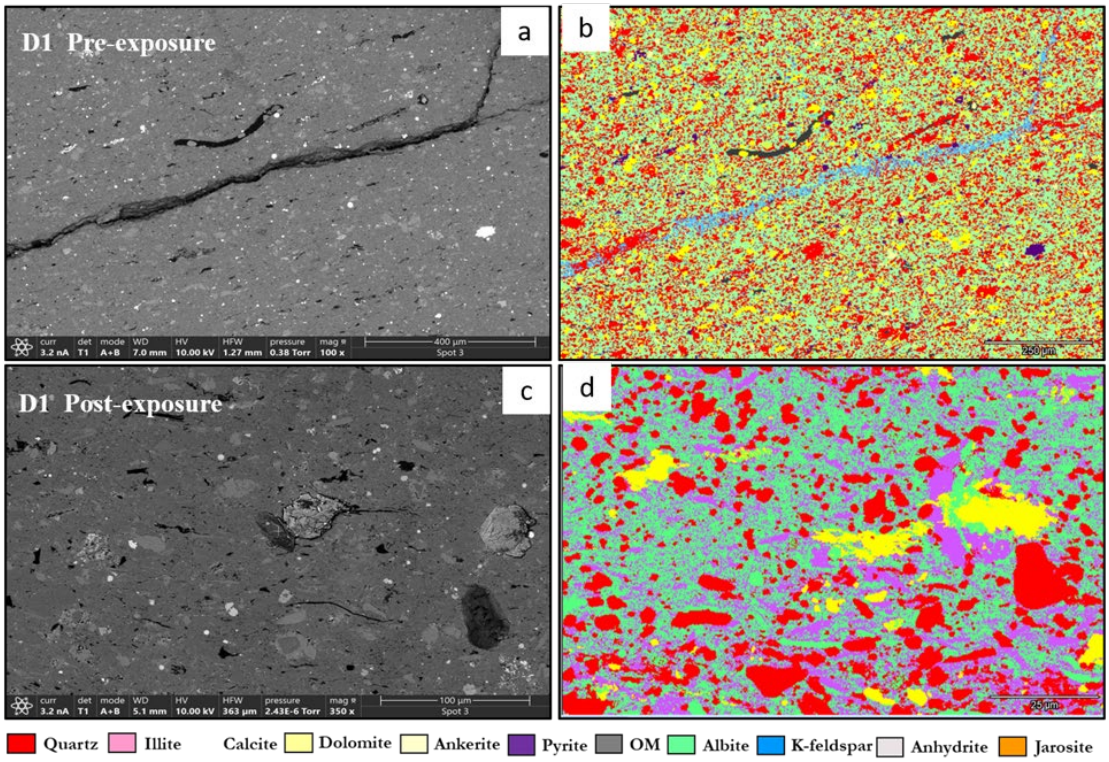

Figure 9. Post-exposure microstructure of caprock facies (D2A) showing illite edge thinning and localized appearance of paragonite. Feldspar grains display surface alteration and incipient etching, especially at clay–feldspar interfaces.

4.1.2. Sulfide Oxidation and Sulfate Reaction Pathways

Formation of jarosite and additional anhydrite ($CaSO_4$) was observed in both reservoir and caprock facies following $scCO_2$ exposure. These phases are associated with pyrite oxidation and redistribution of sulfate from pre-existing anhydrite. Their presence in a closed system, containing only $scCO_2$ and no added SO_2, indicates that sulfate-bearing phases can form under localized oxidative conditions. Co-occurrence with organic matter and likely trace water suggests that redox activity can occur in the absence of externally supplied oxidants, supporting Fe^{2+} and SO_4^{2-} mobility in the various facies [35]. Sulfate-bearing phases, although less frequently emphasized in shale carbon storage contexts, are observed to persist under the experimental conditions. Jarosite was identified in multiple points, and both jarosite and anhydrite are known to exhibit stability under low pH and moderate temperature [36]. Jarosite spikelets as seen in Figure 6, show vast porosity created, giving more room for sequestration. Figure 10 shows the pre and postexposure EDS of the jarosite linked spot. Here, the reaction is hypothesized to initiate through pyrite oxidation, likely accelerated by the presence of trace porewater and redox-active OM [37]. This process releases Fe^{2+} and S^{2-}, which, under oxidizing conditions, transition into Fe^{3+} and SO_4^{2-} [38], ultimately forming jarosite through a precipitation reaction:

$$K^+(aq) + 3Fe^{3+}(aq) + 2SO_4^{2-}(aq) + 6H_2O \rightarrow KFe_3(SO_4)_2(OH)_6(s) + 6H^+(aq) \quad (1)$$

Equation 1 shows the jarosite formation reaction which is thermodynamically favored under acidic, low ionic strength conditions [39]. Its appearance in a brine-free, $scCO_2$ setting underscores the capability of shale-hosted systems to support complex redox mineral transformations without exogenous oxidants. Our results indicate that sulfate mineral formation can occur alongside carbonate reactivity, particularly in organic-rich zones where sulfide-CO_2 interactions are spatially linked.

© 2025 by the author(s). Distributed under a Creative Commons CC BY license.

Preprints.org (www.preprints.org) | NOT PEER-REVIEWED | Posted: 5 June 2025 doi:10.20944/preprints202506.0412.v1

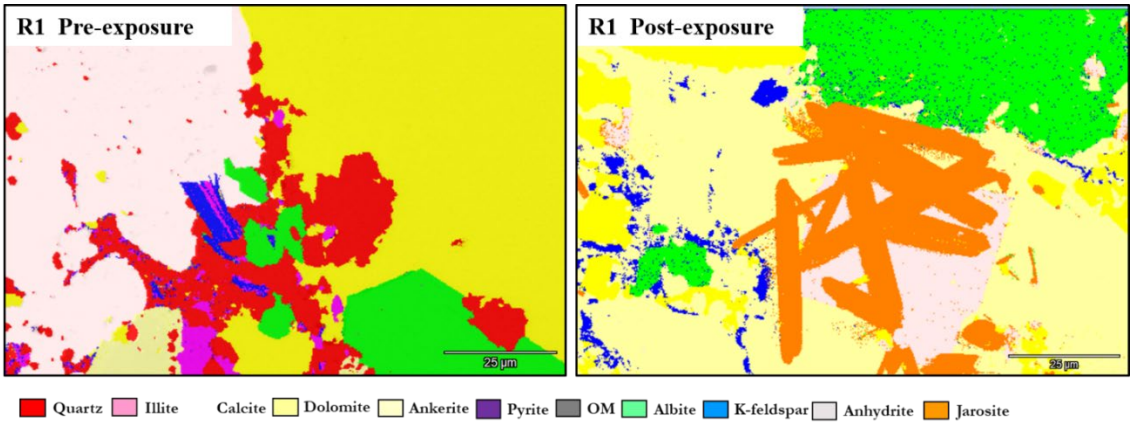

Figure 10. Jarosite formation and sulfate redistribution following scCO₂ exposure. Post-exposure mineral map shows newly formed jarosite in reservoir facies with adjacent porosity development, suggesting sulfate phase persistence under localized oxidative conditions.

4.1.3. Organic Matter: A Chemically Active Interface

Organic matter played a dual role across all facies, two proxies are used in Figure 11. It acted both as a high-affinity sorbent for CO_2 and as a catalytic interface for redox-mediated mineral reactions [41]. In ductile caprock facies, organic surfaces underwent fragmentation and porosity development, which enhanced their ability to store CO_2 in micropores [18]. These changes also supported electron transfer reactions, especially near pyrite and clay edges, fostering the nucleation of new mineral phases [42]. Organic matter can be defined in our context as a chemically active interface. The formation of illite-OM aggregates and secondary mineral patches at OM-clay boundaries confirm that organic matter supports not only CO_2 uptake but also chemical transformation. Previous studies have shown the sorptive value of OM [24], but the current results demonstrate its capacity to induce mineral precipitation and stabilize reaction fronts. This behavior extends the functional relevance of organic matter from passive retention to active geochemical regulation within shale-hosted sequestration systems.

© 2025 by the author(s). Distributed under a Creative Commons CC BY license.

Preprints.org (www.preprints.org) | NOT PEER-REVIEWED | Posted: 5 June 2025 doi:10.20944/preprints202506.0412.v1

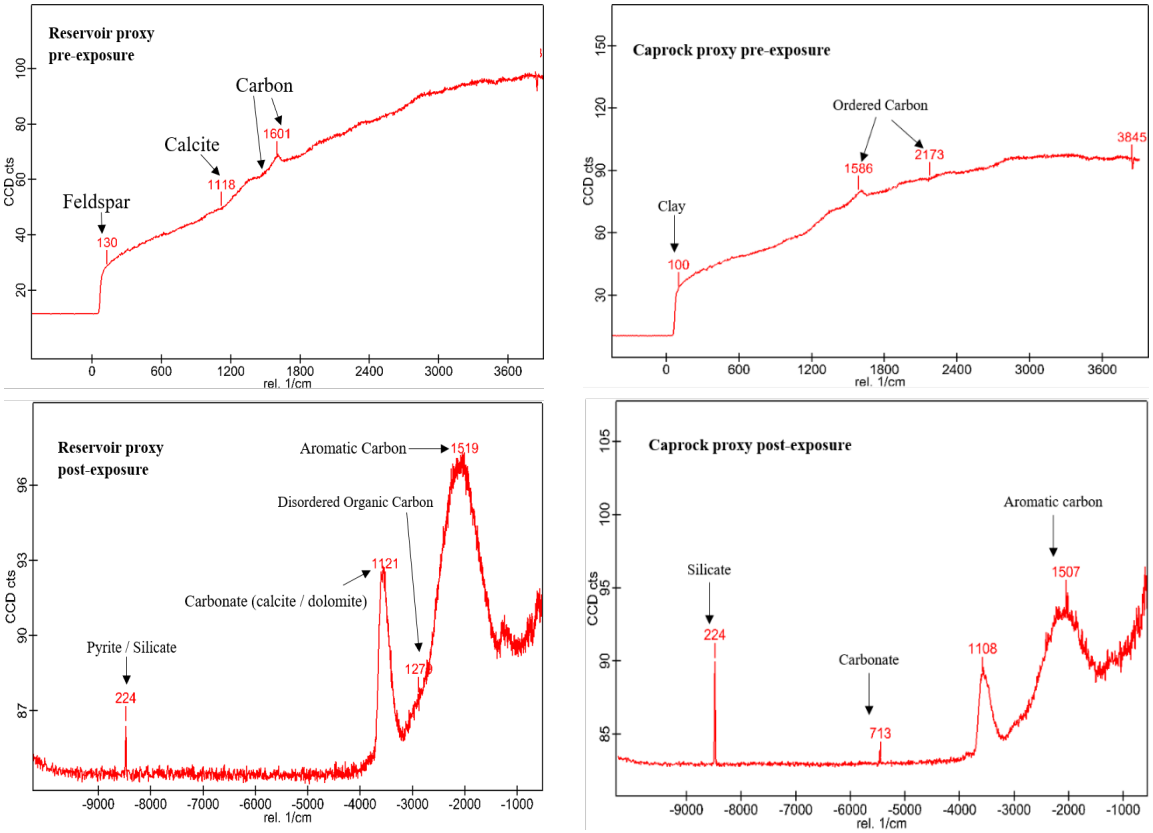

Figure 11. Raman spectra of reservoir and caprock facies (R1) before and after $scCO_2$ exposure. In the reservoir proxy, carbon signals evolve from a broad peak (~1601 cm^{-1}) to separated disordered and aromatic bands (1279 cm^{-1} and 1519 cm^{-1}). In the caprock proxy, a similar transition is observed, with a pre-exposure band at 1586 cm^{-1} shifting to 1507 cm^{-1} post-exposure. Peaks associated with carbonate (~1108–1121 cm^{-1}), silicate (~224 cm^{-1}), and clay (~100–130 cm^{-1}) are also present. Spectra confirm the retention and spectral transformation of organic matter across both facies.

4.2. Relevance for Geochemical Sequestration

The mineral transformations and reactivity patterns observed in this study suggest that Caney Shale facies contribute to CO_2 storage in distinct yet complementary ways. Reservoir units serve as the primary trapping domains through carbonate dissolution and reprecipitation. Ductile caprock facies, on the other hand, operate as chemical seals, limiting vertical migration and stabilizing CO_2 through redox and sulfate-based reactions.

4.2.1. Reservoir Proxies

Proxies R1 through R3 are characterized by high quartz content combined with moderate amounts of reactive carbonates, clays, and organic matter. Spatially localized dissolution and precipitation were observed, primarily concentrated along mineral boundaries and microstructural interfaces. R2 exhibited the most extensive carbonate loss, particularly of ankerite, followed by irregular precipitation of both carbonate and silicate phases. R3, with lower carbonate content, displayed greater expression of organic matter and sulfate reactivity, indicating multiple coexisting trapping mechanisms [29]. Such mineral–fluid interactions align with findings in other mixed-lithology reservoirs, where uneven carbonate distribution contributes significantly to chemical trapping [34]. The detection of Ca–Si-rich areas at silicate–carbonate-OM interfaces suggests the formation of calcium-bearing silicate assemblies [42]. While wollastonite ($CaSiO_3$) was not conclusively identified, Raman and EDS data reveal spatially correlated Ca^{2+} and SiO_2 signals consistent with possible low-crystallinity or transitional Ca–silicate compounds [43]. These mineral

© 2025 by the author(s). Distributed under a Creative Commons CC BY license.

Preprints.org (www.preprints.org) | NOT PEER-REVIEWED | Posted: 5 June 2025 doi:10.20944/preprints202506.0412.v1

associations, though unresolved in structure, may represent additional trapping phases not typically emphasized in standard CCS models [7,43]. Such variability in mineral phases supports localized reactivity that could potentially enhances CO_2 retention in texturally heterogeneous zones. The reservoir proxies are thus accounted for reactive porosity and multiphase trapping.

4.2.2. Caprock Proxies

Caprock proxies D1 and D2 retained structural integrity and low porosity following $scCO_2$ exposure. Their composition rich in clays and organic matter, and the emergence of sealing-associated phases suggest a dominant geochemical sealing role rather than bulk-phase CO_2 mineralization [44]. Compact microtextures were preserved post-exposure, and the presence of sulfate and redox-active phases was confirmed by both SEM-EDS and Raman analyses [43]. These features are consistent with current caprock performance models that emphasize ion retention and interfacial buffering over mechanical deformation. Sulfate mineralization and redox processes involving organic matter occur in the absence of external oxidants or brine immersion. The sealing behavior is reinforced by microscale dissolution–precipitation reactions that operate across reactive boundaries and enhance caprock resilience without compromising structural integrity [45]. These processes are not just passive but actively reinforce sealing through coupled dissolution and precipitation at the microscale. Caprock proxies are thus accounted for ensuring sealing (geochemically proven), hence confirming the dual nature of shales as for CO_2 containment and leak prevention.

4.2.3. Integrated Storage Performance and Relevance for CCS Design

Facies-dependent responses in Caney Shale illustrate the function of an integrated trapping system in which porosity access, geochemical transformation, and redox buffering act concurrently. Reservoir zones enable CO_2 migration and support mineral conversion along carbonate and sulfate pathways. Caprock layers contribute by limiting leakage through chemical immobilization and formation of clay barrier phases at reactive interfaces. Formation of sulfate-bearing minerals, calcium–silicate domains, and clay–organic composites under $scCO_2$ exposure broadens the range of sequestration pathways beyond traditional carbonate-based considerations.

SEM-EDS analyses of Caney Shale samples exposed to $scCO_2$ reveal dual effects: local mineral transformations support both self-sealing and mechanical weakening processes. Carbonate dissolution was frequently accompanied by precipitation of secondary phases at grain boundaries and within pore spaces, especially in reservoir facies such as R2 and R3. These fine-scale precipitates suggest activation of self-sealing pathways, even without brine, aligning with prior findings in clay–carbonate systems [38].

Similarly, microstructural weakening was evident in caprock facies. Illite exhibited sheet-edge thinning and minor delamination; pyrite showed early oxidation; and organic matter displayed fragmentation with increased surface porosity. Such alterations, most prominent in D1 and D2, raise concerns about clay integrity under prolonged exposure, consistent with reported CO_2-induced softening of sealing units under low-water conditions [3]. The interplay between sealing and weakening is spatially variable and phase-dependent. In carbonate-rich zones, reprecipitation may enhance capillary sealing. In phyllosilicate-dominated domains, structural degradation may reduce long-term integrity, particularly under stress cycles associated with injection operations [2,35]. Observed phase transformations support a wider trapping framework that incorporates both primary reactions and secondary mineral development without reliance on brine or supplemental oxidants. Caney Shale demonstrates geochemical and structural reliability for long-term CO_2 retention, with distinct yet complementary contributions from reservoir and caprock settings. Table 3 provides an overview of literature with the common mineral phases associated with CCUS and how they fit the purpose of our research.

© 2025 by the author(s). Distributed under a Creative Commons CC BY license.

Preprints.org (www.preprints.org) | NOT PEER-REVIEWED | Posted: 5 June 2025 doi:10.20944/preprints202506.0412.v1

Table 3. Comparing observed mineralogical changes with CO_2 interactions in shales.

Mineral Phase	Chemical Formula	Rationale in CCUS	Occurrence in Shales	Relevance to CCUS
Calcite	$CaCO_3$	Forms during CO_2 sequestration via reaction with calcium-bearing minerals.	Common carbonate mineral in shales.	Relevant due to carbonate precipitation under CO_2-rich conditions.
Dolomite	$CaMg(CO_3)_2$	Forms from interactions of CO_2 with calcium and magnesium-rich minerals.	Present in some shale formations; associated with carbonate deposits.	Plays a role in carbonate mineralization under CO_2 sequestration.
Magnesite	$MgCO_3$	Forms when CO_2 reacts with magnesium-bearing minerals.	Rare in shales, mainly found in magnesium-rich environments.	Forms stable carbonate phases during CO_2 sequestration.
Siderite	$FeCO_3$	Iron carbonate that forms in CO_2-rich environments.	Occasionally found in Fe-rich shales, but more common in sedimentary rocks.	Can store CO_2 in carbonate form but limited occurrence in shales.
Quartz	SiO_2	Stable silicate mineral in shales, largely unreactive to CO_2.	Common silicate mineral in shales, a major constituent of sandstones.	Mechanically stable but chemically inert under CO_2 exposure.
Illite	$(K,H_3O)(Al,Mg,Fe)_2(Si,Al)_4O_{10}[(OH)_2$	Clay mineral influencing shale porosity and permeability under CO_2 exposure.	Frequent in shales as a clay mineral affecting permeability.	Affects shale permeability and reactivity with CO_2.
Montmorillonite	$(Na,Ca)_{0.3}(Al,Mg)_2Si_4O_{10}(OH)_2 \cdot nH_2O$	Swelling clay mineral that absorbs CO_2, altering shale properties.	Found in clay-rich shales, particularly those with high swelling potential.	Modifies pore structure and water retention upon CO_2 exposure.
Kaolinite	$Al_2Si_2O_5(OH)_4$	Clay mineral with minor interactions with CO_2.	Occurs in some shales but not a dominant mineral.	Minor role in CO_2 reactivity, mainly affects shale composition.
Ankerite	$Ca(Fe^{2+},Mg,Mn)(CO_3)_2$	Iron and magnesium carbonate forming under CO_2 sequestration conditions.	Found in iron-rich sedimentary formations, including some shales.	Potentially relevant for mineral trapping of CO_2.

© 2025 by the author(s). Distributed under a Creative Commons CC BY license.

Preprints.org (www.preprints.org) | NOT PEER-REVIEWED | Posted: 5 June 2025 doi:10.20944/preprints202506.0412.v1

Chlorite	$(Mg,Fe^{2+},Fe^{3+},Al)_6(Si,Al)_4O_{10}(OH)_8$	Clay mineral influencing CO_2-induced alterations in shales.	Occurs in some shales, affecting fluid interactions.	Affects CO_2-rock interactions by modifying clay stability.
Pyrite	FeS_2	Common sulfide in shales, oxidizing under CO_2 influence.	Common in organic-rich shales, particularly those with high sulfur content.	Oxidation influences acid generation, affecting mineral trapping.
Feldspar	$KAlSi_3O_8$ – $NaAlSi_3O_8$ – $CaAl_2Si_2O_8$	Silicate mineral that weathers in CO_2 environments.	Common framework silicate mineral in various shales.	Minor role in CO_2 sequestration; undergoes limited chemical change.
Hematite	Fe_2O_3	Iron oxide that forms from pyrite oxidation during CO_2 sequestration.	Minor iron oxide phase in shales formed from oxidation processes.	May form secondary precipitates upon CO_2 exposure.
Anhydrite	$CaSO_4$	Sulfate mineral present in caprocks affecting CO_2 storage integrity.	Common in evaporite-bearing shales and caprocks.	Contributes to caprock integrity in sequestration sites.
Gypsum	$CaSO_4{\cdot}2H_2O$	Hydrated sulfate mineral influenced by CO_2-rich fluids.	Hydrated form of anhydrite, often found in caprocks overlying shales.	Influences CO_2 migration in formations containing gypsum.
Halite	NaCl	Salt mineral forming low-permeability barriers in caprocks.	Evaporite mineral occasionally present in shale formations.	Enhances caprock sealing potential, reducing CO_2 leakage.
Serpentine	$(Mg,Fe)_3Si_2O_5(OH)_4$	Silicate mineral reacting with CO_2 to form magnesite.	Occurs in some altered shales with high magnesium content.	Can interact with CO_2 under specific geochemical conditions.
Olivine	$(Mg,Fe)_2SiO_4$	Silicate mineral reacting with CO_2 to facilitate mineral sequestration.	Found in ultramafic environments but rare in shales.	Minor direct role in CO_2 sequestration in shales.
Plagioclase	$(Na,Ca)(Si,Al)_4O_8$	Silicate feldspar undergoing carbonation reactions with CO_2.	Common in feldspar-rich shales and sandstones.	Participates in feldspar weathering reactions under CO_2 influence.

© 2025 by the author(s). Distributed under a Creative Commons CC BY license.

Preprints.org (www.preprints.org) | NOT PEER-REVIEWED | Posted: 5 June 2025 doi:10.20944/preprints202506.0412.v1

Smectite	$(Ca,Na)_{0.33}(Al,Mg)_2(Si_4O_{10})(OH)_2 \cdot nH_2O$	Clay group mineral swells upon CO_2 exposure, modifying rock properties.	Occurs in clay-rich shale formations, affecting fluid movement.	Clay swelling may alter CO_2 migration pathways.
Brucite	$Mg(OH)_2$	Magnesium hydroxide that reacts with CO_2 forming magnesite.	Rare in shales but found in magnesium-rich alteration zones.	Relevant in carbonation processes for CO_2 trapping.
Forsterite	Mg_2SiO_4	High-Mg silicate reacting with CO_2 for mineral sequestration.	More common in ultramafic formations, rare in shales.	Limited relevance in shales; reacts with CO_2 in ultramafic rocks.
Talc	$Mg_3Si_4O_{10}(OH)_2$	Magnesium silicate that alters during CO_2 interactions.	Occurs in talc-carbonate altered zones; uncommon in shales.	Plays minor role in mineral transformations in CO_2 storage.
Mariposite	Cr-muscovite	Chromium-bearing mica associated with carbonated ultramafic rocks.	Occasionally found in altered metamorphic environments, rare in shales.	Not directly involved in CO_2 trapping but alters rock properties.
Fuchsite	Cr-muscovite	Green, chromium-bearing mica found in carbonated environments.	Rarely found in shales; more common in metamorphic terrains.	Limited role in CO_2 interactions due to mineral stability.
Zeolites	Mx/n [(AlO2)x(SiO2)y] · zH2O	Adsorbs CO_2, enhancing storage capacity in shales.	Uncommon in natural shale formations but widely used in CO_2 capture studies.	Relevant in artificial CO_2 capture applications but rare in shales.
Muscovite	$KAl_2(AlSi_3O_{10})(OH)_2$	Stable mineral in shales, does not significantly react with CO_2 under sequestration conditions.	Common in shales as a mica mineral, contributing to overall mineral composition.	Minimal role in CO_2 sequestration due to chemical stability.
Jarosite	$KFe_3(SO_4)_2(OH)_6$	Forms in acidic environments and is not relevant for CO_2 sequestration in typical shale formations.	Not common in shales; forms in oxidizing, acidic conditions, often as a sulfide weathering product.	Not relevant for CCUS in shales due to formation constraints.

© 2025 by the author(s). Distributed under a Creative Commons CC BY license.

Preprints.org (www.preprints.org) | NOT PEER-REVIEWED | Posted: 5 June 2025 doi:10.20944/preprints202506.0412.v1

Dawsonite	$NaAlCO_3(OH)_2$	Potential mineral for CO_2 trapping in sandstone formations through carbonate precipitation.	Rare; more common in sandstone reservoirs where CO_2 mineral trapping occurs.	Relevant in sandstone-hosted sequestration but not typically found in shale settings.

4.3. Geochemical Insights

Mineral reactivity in the Caney Shale under $scCO_2$ exposure is highly localized, driven by the spatial arrangement of reactive phases and interfacial microenvironments. Transformations occurred not uniformly, but along grain boundaries where carbonates, clays, sulfides, and organic matter converge. These interfaces enabled coupled processes such as ion exchange, redox cycling, and secondary phase nucleation. Consequently, this extends trapping pathways beyond carbonate dissolution. In Figure 12, illustrations of the observed mineral evolution reflect not just composition, but the connectivity and proximity of reactive constituents in both facieses. Organic matter enhanced reactivity by supporting electron transfer and acting as a nucleation site, while stable phases like quartz and feldspar constrained reactions spatially. Overall, trapping efficiency in the Caney Shale appears controlled less by bulk mineralogy than by the distribution and interaction of components at the microscale.

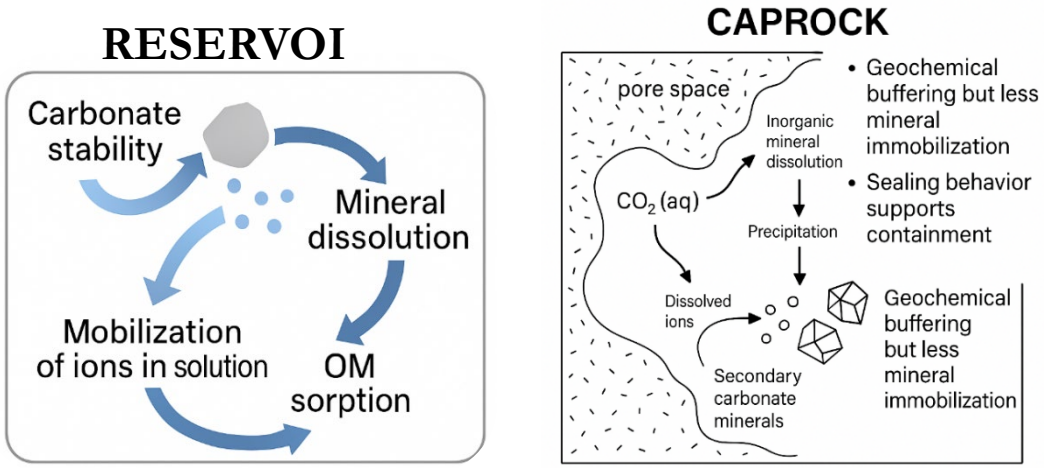

(**a**) (**b**)

Figure 12. Shale exhibits dual-functionality for CO_2 storage governed by facies-specific geochemical behavior. (a) The reservoir acts as a reactive matrix, promoting mineral dissolution, elemental redistribution, and stable secondary phase precipitation essential for geochemical trapping. (b) The caprock maintains low reactivity, enabling structural preservation through limited transformation and clay-stabilization, thereby supporting long-term seal integrity.

5. Conclusions

Exposure of Caney Shale to pure $scCO_2$ at 60 °C and 2500 psia induces rapid, phase-specific mineral reactions relevant to long-term carbon storage. Quartz remains chemically inert, while carbonates dissolve and locally reprecipitate as calcium- and iron-rich secondary phases. Illite exhibits edge alteration and cation leaching; pyrite undergoes early-stage oxidation; and organic matter becomes more porous, supporting redox activity at mineral interfaces. SEM-EDS analysis confirms that mineral trapping initiates under dry conditions, with nanometer-scale precipitates forming at grain boundaries and pore surfaces. Reactions are not uniformly distributed but are

© 2025 by the author(s). Distributed under a Creative Commons CC BY license.

Preprints.org (www.preprints.org) | NOT PEER-REVIEWED | Posted: 5 June 2025 doi:10.20944/preprints202506.0412.v1

instead governed by spatial variability in mineral associations, surface properties, and interface geochemistry. Insights gained from this experiment includes:

- Localized porosity development enhances CO_2 injectivity, while secondary mineral precipitation at grain contacts and pore throats contributes to self-sealing behavior, supporting containment stability.
- Demonstrated mineral trapping in dry scCO_2 (no added brines) systems confirms that water is not a prerequisite for initiating geochemical containment, with in situ precipitation providing a viable mechanism for immobilizing (sequestering) injected CO_2.
- Facies-dependent reactivity, mineral phase and ionic species distribution support a naturally evolving balance between fluid migration pathways and geochemical seals. This allows reactive zones (reservoirs) to co-exist with stable, low-permeability zones (caprocks).
- Existing shale development from hydraulic fracturing offers an operational advantage, enabling CO_2 storage to leverage established well infrastructure, reservoir access strategies, and field-scale monitoring systems.

Future work should explore sulfate phase formation, including jarosite ($KFe_3(OH)_6(SO_4)_2$), using combined with reactive-transport modeling and calculations. Integrating EDS-based stoichiometries with kinetic datasets will help quantify CO_2 uptake across key mineral phases. Extending experiments to other shales will provide a crosslink benchmarking. Incorporating mineral-scale reaction rates into geomechanical and geophysical models can improve leakage-risk assessments, while EBSD and FIB-SEM will enable deeper characterization of reaction zones and deformation below the surface. These steps will sharpen monitoring strategies, and ultimately strengthen confidence in shale-dominated formations as long-term, self-adjusting CO_2 sequesters.

Author Contributions: Conceptualization, M.R. and L.B.D; methodology, L.B.D.; software, X.X.; validation, L.B.D and M.R.; formal analysis, L.B.D.; investigation, L.B.D..; resources, M.R..; data curation, L.B.D, M.R.; writing—original draft preparation, L.B.D.; writing—review and editing, L.B.D and M.R.; visualization, L.B.D.; supervision, M.R..; project administration, M.R.; funding acquisition, M.R. All authors have read and agreed to the published version of the manuscript.

Funding: This research received no external funding and the samples were part of the former project funded by US Department of Energy, grant Award DEFE0031776 from the Office of Fossil Energy's, Oil and Natural Gas Program.

Data Availability Statement: We encourage all authors of articles published in MDPI journals to share their research data. In this section, please provide details regarding where data supporting reported results can be found, including links to publicly archived datasets analyzed or generated during the study. Where no new data were created, or where data is unavailable due to privacy or ethical restrictions, a statement is still required. Suggested Data Availability Statements are available in section "MDPI Research Data Policies" at https://www.mdpi.com/ethics.

Acknowledgments: The authors would like to acknowledge Dr. Jim Puckette for training and granting access to his laboratory space and equipment for sample preparation; Mr. Brent Johnson and Ms. Lisa Whitworth, for training and assistance during materials characterization at the OSU Microscopy Lab; All the members of the Barrier Materials and Geomimicry lab: Dr Ali Ettehadi, Bruce Mutume and Brady Chenoweth, for being a daily motivation and inspiration.

Conflicts of Interest: The authors declare no conflicts of interest. The funders had no role in the design of the study; in the collection, analyses, or interpretation of data; in the writing of the manuscript; or in the decision to publish the results.

References

1. Ndlovu, P.; Bulannga, R.; Mguni, L.L. Progress in Carbon Dioxide Capture, Storage and Monitoring in Geological Landform. *Front. Energy Res.* **2024**, *12*, 1450991, doi:10.3389/fenrg.2024.1450991.

© 2025 by the author(s). Distributed under a Creative Commons CC BY license.

Preprints.org (www.preprints.org) | NOT PEER-REVIEWED | Posted: 5 June 2025 doi:10.20944/preprints202506.0412.v1

2. Olabode, A.; Radonjic, M. Characterization of Shale Cap-Rock Nano-Pores in Geologic CO_2 Containment. *Environmental & Engineering Geoscience* **2014**, *20*, 361–370, doi:10.2113/gseegeosci.20.4.361.
3. Busch, A..; Amann, A..; Bertier, P..; Waschbusch, M..; Krooss, B.M. The Significance of Caprock Sealing Integrity for CO_2 Storage. In Proceedings of the All Days; SPE: New Orleans, Louisiana, USA, November 10 2010; p. SPE-139588-MS.
4. Du, H.; Carpenter, K.; Hui, D.; Radonjic, M. Microstructure and Micromechanics of Shale Rocks: Case Study of Marcellus Shale. *Facta Universitatis, Series: Mechanical Engineering* **2017**, *15*, 331–340, doi:10.22190/FUME170602016D.
5. Hazra, B.; Vishal, V.; Sethi, C.; Chandra, D. Impact of Supercritical CO_2 on Shale Reservoirs and Its Implication for CO_2 Sequestration. *Energy Fuels* **2022**, *36*, 9882–9903, doi:10.1021/acs.energyfuels.2c01894.
6. Wang, Y.; Luo, G.; Achang, M.; Cains, J.; Wethington, C.; Katende, A.; Grammer, G.M.; Puckette, J.; Pashin, J.; Castagna, M.; et al. Multiscale Characterization of the Caney Shale — An Emerging Play in Oklahoma. *Midcontinent Geoscience* **2021**, *2*, 33–53, doi:10.17161/mg.v2i.15911.
7. Xie, W.; Chen, S.; Wang, M.; Yu, Z.; Wang, H. Progress and Prospects of Supercritical CO_2 Application in the Exploitation of Shale Gas Reservoirs. *Energy Fuels* **2021**, *35*, 18370–18384, doi:10.1021/acs.energyfuels.1c02944.
8. Huang, Y.; Liu, F.; Kang, Y.; Hu, Y.; Liu, Y. SC-CO_2 and Brine Exposure Altering the Mineralogy, Microstructure, and Micro- and Macromechanical Properties of Shale. *Energy Fuels* **2024**, *38*, 11064–11077, doi:10.1021/acs.energyfuels.4c01637.
9. Tapriyal, D.; Haeri, F.; Crandall, D.; Horn, W.; Lun, L.; Lee, A.; Goodman, A. Caprock Remains Water Wet Under Geologic CO2 Storage Conditions. *Geophysical Research Letters* **2024**, *51*, e2024GL109123, doi:10.1029/2024GL109123.
10. Katende, A.; Awejori, G.; Benge, M.; Nakagawa, S.; Wang, Y.; Xiong, F.; Puckette, J.; Grammer, M.; Rutqvist, J.; Doughty, C.; et al. Multidimensional, Experimental and Modeling Evaluation of Permeability Evolution, the Caney Shale Field Lab, OK, USA. In *Unconventional Resources Technology Conference, 13?15 June 2023*; SEG Global Meeting Abstracts; Unconventional Resources Technology Conference (URTeC), 2023; pp. 1505–1526.
11. Sori, A.; Moghaddas, J.; Abedpour, H. Comprehensive Review of Experimental Studies, Numerical Modeling, Leakage Risk Assessment, Monitoring, and Control in Geological Storage of Carbon Dioxide: Implications for Effective CO2 Deployment Strategies. *Greenhouse Gases: Science and Technology* **2024**, *14*, 887–913, doi:10.1002/ghg.2295.
12. Ehlig-Economides, C.A. Geologic Carbon Dioxide Sequestration Methods, Opportunities, and Impacts. *Current Opinion in Chemical Engineering* **2023**, *42*, 100957, doi:10.1016/j.coche.2023.100957.
13. Wang, L.; Zhang, Y.; Zou, R.; Zou, R.; Huang, L.; Liu, Y.; Meng, Z.; Wang, Z.; Lei, H. A Systematic Review of CO2 Injection for Enhanced Oil Recovery and Carbon Storage in Shale Reservoirs. *International Journal of Hydrogen Energy* **2023**, *48*, 37134–37165, doi:10.1016/j.ijhydene.2023.06.099.
14. Fitts, J.P.; Peters, C.A. Caprock Fracture Dissolution and CO2 Leakage. *Reviews in Mineralogy and Geochemistry* **2013**, *77*, 459–479, doi:10.2138/rmg.2013.77.13.
15. Olabode, A.; Radonjic, M. Shale Caprock/Acidic Brine Interaction in Underground CO2 Storage. *Journal of Energy Resources Technology* **2014**, *136*, doi:10.1115/1.4027567.
16. Zhou, J.; Tian, S.; Xian, X.; Zheng, Y.; Yang, K.; Liu, J. Comprehensive Review of Property Alterations Induced by CO2–Shale Interaction: Implications for CO2 Sequestration in Shale. *Energy Fuels* **2022**, *36*, 8066–8080, doi:10.1021/acs.energyfuels.2c01542.
17. Anderson, S.T.; Jahediesfanjani, H. Estimating the Pressure-Limited Dynamic Capacity and Costs of Basin-Scale CO2 Storage in a Saline Formation. *International Journal of Greenhouse Gas Control* **2019**, *88*, 156–167, doi:10.1016/j.ijggc.2019.05.031.
18. Liu, Q.; Sun, M.; Sun, X.; Liu, B.; Ostadhassan, M.; Huang, W.; Chen, X.; Pan, Z. Pore Network Characterization of Shale Reservoirs through State-of-the-Art X-Ray Computed Tomography: A Review. *Gas Science and Engineering* **2023**, *113*, 204967, doi:10.1016/j.jgsce.2023.204967.

© 2025 by the author(s). Distributed under a Creative Commons CC BY license.

Preprints.org (www.preprints.org) | NOT PEER-REVIEWED | Posted: 5 June 2025 doi:10.20944/preprints202506.0412.v1

19. Gao, H.; Xie, Y.; Cheng, Z.; Wang, C.; Li, T.; Zhu, X.; Luo, K.; Cao, J.; Li, N. A Minireview of the Influence of CO2 Injection on the Pore Structure of Reservoir Rocks: Advances and Outlook. *Energy Fuels* **2023**, *37*, 118–135, doi:10.1021/acs.energyfuels.2c03328.
20. Fentaw, J.W.; Emadi, H.; Hussain, A.; Fernandez, D.M.; Thiyagarajan, S.R. Geochemistry in Geological CO2 Sequestration: A Comprehensive Review. *Energies* **2024**, *17*, 5000, doi:10.3390/en17195000.
21. Wang, J.; Wang, K.; Shan, X.; Taylor, K.G.; Ma, L. Potential for CO2 Storage in Shale Basins in China. *International Journal of Greenhouse Gas Control* **2024**, *132*, 104060, doi:10.1016/j.ijggc.2024.104060.
22. Shukla, R.; Ranjith, P.; Haque, A.; Choi, X. A Review of Studies on CO2 Sequestration and Caprock Integrity. *Fuel* **2010**, *89*, 2651–2664, doi:10.1016/j.fuel.2010.05.012.
23. Leng, J.; Bump, A.; Hosseini, S.A.; Meckel, T.A.; Wang, Z.; Wang, H. A Comprehensive Review of Efficient Capacity Estimation for Large-Scale CO2 Geological Storage. *Gas Science and Engineering* **2024**, *126*, 205339, doi:10.1016/j.jgsce.2024.205339.
24. Dong, M.; Gong, H.; Sang, Q.; Zhao, X.; Zhu, C. Review of CO2-Kerogen Interaction and Its Effects on Enhanced Oil Recovery and Carbon Sequestration in Shale Oil Reservoirs. *Resources Chemicals and Materials* **2022**, *1*, 93–113, doi:10.1016/j.recm.2022.01.006.
25. Kelemen, P.; Benson, S.M.; Pilorgé, H.; Psarras, P.; Wilcox, J. An Overview of the Status and Challenges of CO2 Storage in Minerals and Geological Formations. *Front. Clim.* **2019**, *1*, doi:10.3389/fclim.2019.00009.
26. Carpenter, K.C.; Dje, L.B.; Achang, M.; Radonjic, M. Comparative Laboratory Study of the Geochemical Reactivity of the Marcellus Shale: Rock–Fluid Interaction of Drilled Core Samples vs. Outcrop Specimens. *Water* **2023**, *15*, 1940, doi:10.3390/w15101940.
27. Chang, X.; Lin, S.; Yang, C.; Wang, K.; Liu, S.; Guo, Y. A Critical Review of ScCO2-Enhanced Gas Recovery and Geologic Storage in Shale Reservoirs. *Gas Science and Engineering* **2024**, *125*, 205317, doi:10.1016/j.jgsce.2024.205317.
28. Awejori, G.A.; Dong, W.; Doughty, C.; Spycher, N.; Radonjic, M. Mineral and Fluid Transformation of Hydraulically Fractured Shale: Case Study of Caney Shale in Southern Oklahoma. *Geomech. Geophys. Geo-energ. Geo-resour.* **2024**, *10*, 128, doi:10.1007/s40948-024-00835-0.
29. Adua Awejori, G.; Doughty, C.; Xiong, F.; Paronish, T.; Spycher, N.; Radonjic, M. Integrated Experimental and Modeling Study of Geochemical Reactions of Simple Fracturing Fluids with Caney Shale. *Energy Fuels* **2022**, *36*, 10064–10081, doi:10.1021/acs.energyfuels.2c01739.
30. Goodman, A.; Fukai, I.; Dilmore, R.; Frailey, S.; Bromhal, G.; Soeder, D.; Gorecki, C.; Peck, W.; Rodosta, T.; Guthrie, G. Methodology for Assessing CO2 Storage Potential of Organic-Rich Shale Formations. *Energy Procedia* **2014**, *63*, 5178–5184, doi:10.1016/j.egypro.2014.11.548.
31. Fatah, A.; Bennour, Z.; Ben Mahmud, H.; Gholami, R.; Hossain, M.M. A Review on the Influence of CO2/Shale Interaction on Shale Properties: Implications of CCS in Shales. *Energies* **2020**, *13*, 3200, doi:10.3390/en13123200.
32. Knauss, K.G.; Johnson, J.W.; Steefel, C.I. Evaluation of the Impact of CO2, Co-Contaminant Gas, Aqueous Fluid and Reservoir Rock Interactions on the Geologic Sequestration of CO2. *Chemical Geology* **2005**, *217*, 339–350, doi:10.1016/j.chemgeo.2004.12.017.
33. Peter, A.; Yang, D.; Eshiet, K.I.-I.I.; Sheng, Y. A Review of the Studies on CO2–Brine–Rock Interaction in Geological Storage Process. *Geosciences* **2022**, *12*, 168, doi:10.3390/geosciences12040168.
34. Sanguinito, S.; Goodman, A.; Tkach, M.; Kutchko, B.; Culp, J.; Natesakhawat, S.; Fazio, J.; Fukai, I.; Crandall, D. Quantifying Dry Supercritical CO2-Induced Changes of the Utica Shale. *Fuel* **2018**, *226*, 54–64, doi:10.1016/j.fuel.2018.03.156.
35. Li, S.; Zhang, S.; Xing, H.; Zou, Y. CO2–Brine–Rock Interactions Altering the Mineralogical, Physical, and Mechanical Properties of Carbonate-Rich Shale Oil Reservoirs. *Energy* **2022**, *256*, 124608, doi:10.1016/j.energy.2022.124608.
36. Zhou, X.; Sang, S.; Niu, Q.; Zhang, K.; Liu, F.; Wang, W.; Chang, J. Changes of Multiscale Surface Morphology and Pore Structure of Mudstone Associated with Supercritical CO_2 -Water Exposure at Different Times. *Energy Fuels* **2021**, *35*, 4212–4223, doi:10.1021/acs.energyfuels.0c03920.

© 2025 by the author(s). Distributed under a Creative Commons CC BY license.

Preprints.org (www.preprints.org) | NOT PEER-REVIEWED | Posted: 5 June 2025 doi:10.20944/preprints202506.0412.v1

37. Choo, T.K.; Etschmann, B.; Selomulya, C.; Zhang, L. Behavior of Fe2+/3+ Cation and Its Interference with the Precipitation of Mg2+ Cation upon Mineral Carbonation of Yallourn Fly Ash Leachate under Ambient Conditions. *Energy Fuels* **2016**, *30*, 3269–3280, doi:10.1021/acs.energyfuels.5b02867.
38. Stubbs, A.R.; MacDonald, J.; Neill, I. Mechanisms of Secondary Carbonate Precipitation on Felsic, Intermediate, and Mafic Igneous Rocks: A Case Study for NW Scotland 2024.
39. Olabode, A.; Radonjic, M. Geochemical Markers in Shale-CO2 Experiment at Core Scale. *Energy Procedia* **2017**, *114*, 3840–3854, doi:10.1016/j.egypro.2017.03.1516.
40. Dje, L.B.; Awejori, G.A.; Radonjic, M. Comparison of Geochemical Reactivity of Marcellus and Caney Shale Based on Effluent Analysis. In Proceedings of the 58th U.S. Rock Mechanics/Geomechanics Symposium; ARMA: Golden, Colorado, USA, June 23 2024; p. D041S053R004.
41. Ghosh, S.; Adsul, T.; Varma, A.K. Organic Matter and Mineralogical Acumens in CO2 Sequestration. In *Green Sustainable Process for Chemical and Environmental Engineering and Science*; Inamuddin, Dr., Altalhi, T., Eds.; Elsevier, 2023; pp. 561–594 ISBN 978-0-323-99429-3.
42. Zhou, Q.; Liu, J.; Ma, B.; Li, C.; Xiao, Y.; Chen, G.; Lyu, C. Pyrite Characteristics in Lacustrine Shale and Implications for Organic Matter Enrichment and Shale Oil: A Case Study from the Triassic Yanchang Formation in the Ordos Basin, NW China. *ACS Omega* **2024**, *9*, 16519–16535, doi:10.1021/acsomega.4c00259.
43. Katende, A.; Rutqvist, J.; Benge, M.; Seyedolali, A.; Bunger, A.; Puckette, J.O.; Rhin, A.; Radonjic, M. Convergence of Micro-Geochemistry and Micro-Geomechanics towards Understanding Proppant Shale Rock Interaction: A Caney Shale Case Study in Southern Oklahoma, USA. *Journal of Natural Gas Science and Engineering* **2021**, *96*, 104296, doi:10.1016/j.jngse.2021.104296.

Disclaimer/Publisher's Note: The statements, opinions and data contained in all publications are solely those of the individual author(s) and contributor(s) and not of MDPI and/or the editor(s). MDPI and/or the editor(s) disclaim responsibility for any injury to people or property resulting from any ideas, methods, instructions or products referred to in the content.

© 2025 by the author(s). Distributed under a Creative Commons CC BY license.